ACCSCIENCE PUBLISHING

International Journal of Bioprinting

RESEARCH ARTICLE

Investigation of humidity-driven swelling–shrinking behavior of filaments in material extrusion of medical-grade biodegradable hydrogel

Kaicheng Yu[1,2†], Yifeng Yao[1,2†], Qiang Gao[1,2*], Le Xu[1,2], Wei Zhang[3], Min Zhu[4], Peng Zhang[1,2], Swee Leong Sing[5*], and Lihua Lu[1,2*]

[1]School of Mechatronics Engineering, Harbin Institute of Technology, Harbin, Heilongjiang, China

[2]Chongqing Research Institute of HIT, Chongqing, China

[3]Key Laboratory of Data Analytics and Optimization for Smart Industry, Northeastern University, Shenyang, Liaoning, China

[4]School of Electrical Engineering and Automation, Harbin Institute of Technology, Harbin, Heilongjiang, China

[5]Department of Mechanical Engineering, College of Design and Engineering, National University of Singapore, Singapore

(This article belongs to *the Special Issue: Advances in 3D Bioprinting*)

[†]These authors contributed equally to this work.

***Corresponding authors:**
Qiang Gao (gaoq@hit.edu.cn)

Swee Leong Sing (sweeleong.sing@nus.edu.sg)

Lihua Lu (lihual@hit.edu.cn)

Citation: Yu K, Yao Y, Gao Q, *et al*. Investigation of humidity-driven swelling–shrinking behavior of filaments in material extrusion of medical-grade biodegradable hydrogel. *Int J Bioprint*. 2025;11(4):409-425. doi: 10.36922/IJB025220222

Received: May 27, 2025
Revised: June 18, 2025
Accepted: June 29, 2025
Published online: June 30, 2025

Abstract

Material extrusion using medical-grade biodegradable hydrogel demonstrates significant potential for manufacturing biocompatible scaffolds in regenerative medicine. However, unpredictable geometric variations in the fabricated models, such as swelling or shrinking, impede the development of complex three-dimensional (3D) hydrogel architectures for *in vitro*-functionalized tissues and organs. A primary cause of structural deformation, such as wrinkling or even collapse, is improper humidity control during the 3D printing process. Therefore, there is a need to investigate the swelling–shrinking behavior of hydrogels under varying ambient humidity and to determine optimal humidity levels for the printing process. This study established a thermal–humidity–multiphase flow coupling field simulation model to numerically investigate the humidity-driven swelling–shrinking behavior of hydrogel filaments. The optimal 3D printing humidity levels were determined for hydrogel filaments with diameters of 0.2, 0.3, and 0.4 mm, which were found to be 90, 80, and 60%, respectively. Using these humidity settings, several structures were fabricated, demonstrating moderated moisture loss of 3D architecture. Notably, a human ear model was successfully printed, achieving an effective size of 20 mm (length) × 10 mm (width) × 10 mm (height). Our research can benefit the future development in tissue engineering and regenerative medicine.

Keywords: 3D printing; Coupling field simulation; Humidity control; Medical hydrogel

1. Introduction

Recently, three-dimensional (3D) printing has emerged as a promising technique in tissue engineering and regenerative medicine,[1,2] driving significant advancements in the fabrication of *in vitro*-functionalized tissues and organs.[3,4] Through this additive manufacturing technology, biomimetic 3D architectures with complex geometric structures can be created using a variety of biocompatible materials.[5,6]

Material extrusion,[7,8] material jetting,[9,10] and vat photopolymerization[11,12] are three well-established 3D printing technologies for fabricating human-scale organs and physiologically relevant disease models. Of these, material extrusion has garnered increasing attention due to its cost-effectiveness and ease of operation.[13,14] The 3D printing process is typically actuated by mechanical force or pneumatic pressure, and the materials are extruded from a fine nozzle. Well-arranged filaments are then deposited on a two-axis substrate along a predefined trajectory.[15,16] Subsequently, a 3D biomimetic architecture is constructed through layer-by-layer deposition.

Currently, medical-grade biodegradable hydrogels have become well-acclaimed bio-inks adopted in material extrusion.[17] These hydrogels closely mimic the biochemical and physical properties of the native extracellular matrix, offering advantages for regenerative medical applications,[18] such as excellent biocompatibility, prominent drug-encapsulating capability, and negligible cytotoxicity.[19] This makes hydrogel materials highly promising candidates for developing tissue engineering scaffolds as delivery vehicles for biologically active substances or cells.[20]

However, as hydrogels are water-insoluble 3D polymeric networks that retain large volumes of fluid, they demonstrate pronounced humidity-driven swelling–shrinking behavior.[21] A wealth of biodegradable hydrogels, such as Pluronic F-127 (F-127), poly(ethylene glycol) diacrylate (PEG-DA), and polyvinyl alcohol (PVA), demonstrate uncontrollable swelling–shrinking behavior when the ambient humidity is unstable. This high susceptibility to the ambient humidity variation often leads to unpredictable geometric sizes in 3D bioprinted structures, which may alter their physical properties. Therefore, humidity control has emerged as a significant parameter in hydrogel-based 3D printing. For example, Chang et al.[22] fabricated a multicomponent 3D structure of micro-vessel fragments using F-127 with a material extrusion device and highlighted humidity as a significant parameter in ensuring the precise deposition of hydrogel and maintaining the structural fidelity of printed architectures. Similarly, Lv et al.[23] created a 3D-printed architecture with stomata-like microstructures using PEG-DA hydrogel, where regulated humidity induced geometric variations that enabled the opening and closing functions of rhombus-shaped stomata. Dai et al.[24] prepared a humidity-driven, dynamically colorful display platform via material extrusion of PVA hydrogel. The platform's optical properties could be modulated by the humidity-driven swelling behavior of the hydrogel, enabling a controllable color of the 3D-printed platform. Additionally, Sun et al.[25] developed a 3D-printed, flexible humidity sensor with a composite of carbon nanotubes, polyaniline, and gelatin. In this system, changes in humidity induced deformation of the gelatin hydrogel, resulting in detectable variation in the electrical resistance of the composite material.

Although there is a broad consensus that humidity plays a crucial role in 3D-printed hydrogel architectures, identifying optimal humidity conditions for hydrogel 3D printing remains challenging. During the extrusion process, continuous hydrogel filaments are deposited onto a plate and remain exposed to ambient air until the 3D structure is fabricated. As water constitutes the majority of hydrogel volume, any variation in moisture content directly impacts the geometry of the 3D-printed filaments.[26]

When 3D printing occurs under inappropriate ambient humidity, the concentration of water in the ambient air is remarkably lower than that within the hydrogel filaments. This disparity causes moisture to evaporate from the surface of filaments, as water diffuses outward and transforms into vapor. The resulting moisture loss leads to filament shrinkage. In contrast, if the ambient humidity is excessively high, moisture from the ambient air may diffuse back into the hydrogel, increasing its water content and causing filament swelling.[27] Such humidity-driven geometric variations often cause deviations from the predefined 3D-printed filaments. These cumulative errors during layer-by-layer deposition can lead to wrinkling or even collapse of the fabricated architecture, ultimately rendering it unsuitable for medical applications.

These challenges hinder the reliable fabrication of biomimetic hydrogel architectures, thereby making the manufacture of functional human-scale tissue or organs impractical.[28] To address these problems, efforts have been made in recent research. For example, Search et al.[29] developed a humidity-controlled chamber capable of maintaining constant humidity levels from 25 to 80%, enabling more stable hydrogel 3D printing conditions. Matamoros et al.[30] prepared an atmospheric chamber to accommodate a self-designed 3D printing device, in which humidity was precisely controlled to maintain the geometry of the 3D-printed architectures. Likewise, Yu et al.[31] proposed a humidity-controlled enclosure for regulating ambient humidity distribution during

hydrogel 3D printing, maintaining levels above 70% to prevent the shrinkage and collapse of the 3D-printed hydrogel structures.

Although prior studies have attempted to regulate ambient humidity during hydrogel 3D printing, most efforts—including the work by Yu et al.[31]—have primarily focused on the external environmental control of the printing space. Specifically, they proposed a humidity-controlled atmospheric enclosure and developed a fluid–thermal–humidity coupled finite element method (FEM) model to simulate the spatial distribution of humidity within the printing chamber. This strategy successfully improved macro-scale environmental stability and reduced the likelihood of structure collapse caused by low humidity. However, their approach only addresses the ambient airfield and does not account for the behavior of individual hydrogel filaments under humidity fluctuations at the material level. In particular, the internal diffusion of water within hydrogel filaments, the associated volumetric deformation, and the interface-driven geometric evolution remain unmodeled. Consequently, their framework is incapable of predicting localized distortion, interlayer error accumulation, or structure failure due to filament-scale swelling and shrinkage.

However, the omission of humidity-driven swelling–shrinking behavior of 3D-printed hydrogel filaments in prior studies has critically limited the advancement of hydrogel-based 3D printing and hindered progress toward reliable biomanufacturing. During the hydrogel printing process, local humidity exerts a significant impact on the geometric variation of fabricated hydrogel models. To preserve the shape of 3D-printed hydrogel constructs, the ambient humidity must be precisely regulated to an optimal level.

Existing research generally focuses on the invention of novel humidity-controlled devices[29–31] to precisely regulate the ambient humidity of 3D-printed structures. However, these studies typically rely on the trial-and-error method to identify optimal humidity levels, a method that is time-consuming, lacks reliability, and suffers from poor repeatability. Such limitations fall short of meeting the requirements for manufacturing biomimetic 3D architectures.

The 3D printing of biomimetic scaffolds aims to produce a range of complex 3D architectures that accurately replicate the natural structure of human tissues and organs.[32] Given the tremendous difference in the sizes of various tissues and organs, hydrogel filaments of varying diameters are often required during the printing process. For example, 3D architectures with larger volumes usually consist of thicker filaments to provide a better load-bearing property,[33] while thinner filaments are generally adopted for smaller constructs to achieve a higher resolution.[34] In such complex circumstances, identifying an optimal humidity level for hydrogel 3D printing becomes increasingly challenging. Therefore, there is an urgent need to investigate the humidity-driven swelling–shrinking behavior of 3D-printed hydrogel filaments.

In this study, the influence of ambient humidity during the 3D printing process on the swelling–shrinking behavior of 3D-printed hydrogel filaments was investigated through numerical simulations and experimental validation. A two-phase flow simulation model, coupled with heat transfer and water vapor transport, was developed based on FEM. The geometric variation of hydrogel filaments with various diameters under varying humidity conditions was estimated, and the optimal humidity levels for hydrogel 3D printing were identified. Subsequently, a series of 3D printing trials was conducted using hydrogel materials with and without the optimal ambient humidity. The results demonstrated that the shrinkage of filaments and the collapse of fabricated 3D architectures were effectively prevented by maintaining the humidity at an optimal level.

2. Materials and methods

This study proposed a 2D thermal–humidity–multiphase flow coupling field simulation model for humidity-driven swelling–shrinking behavior of hydrogel filaments.

In the 3D printing of hydrogel structures, well-arranged filaments were smoothly deposited. The local humidity within the printing space plays a significant role in influencing the geometric variation of these hydrogel filaments. To accurately regulate the humidity field within the printing space, a novel configuration of an extrusion-based 3D printer (SIA bioprinter PRO, Shenyang Institute of Automation, China) was employed, as demonstrated in Figure 1. The feasibility and reliability of this setup were validated in previous research.[31] The 3D printing device comprises a temperature-controlled horizontal plate and a humidity-controlled atmospheric enclosure. During the printing process, the print head operates within this enclosure, allowing the humidity in the printing space to be precisely maintained at a constant value.

2.1. Finite element method modeling for the printed filament

To estimate the humidity-driven swelling–shrinking behavior of printed filaments, a two-phase flow simulation model coupled with heat transfer and water vapor transport was developed using COMSOL Multiphysics 6.2 (COMSOL, USA). Mechanical components not directly interacting with the printed filament, such as the

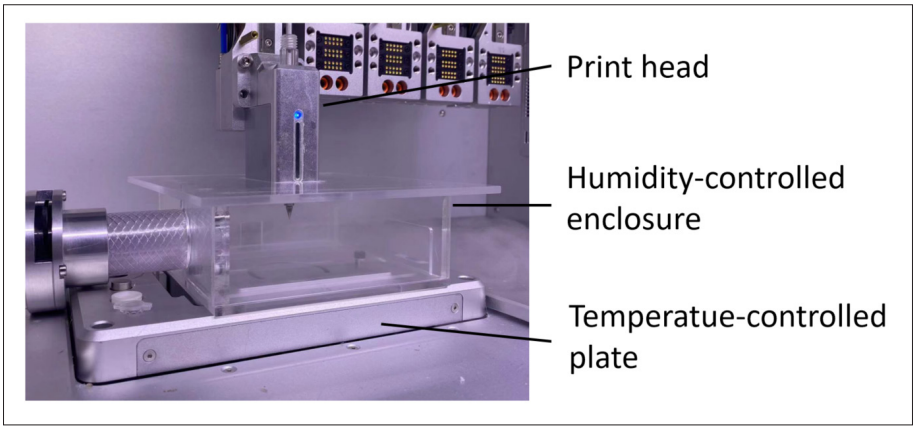

Figure 1. A high-precision 3D printing device with controllable humidity in the printing space.

humidity-controlled enclosure and the 3D print head, were excluded from the analysis. During the material extrusion process, continuous filaments with uniform diameters were extruded from a circular nozzle. Due to gravitational effects, a compressive deformation occurred at the bottom of each filament upon deposition on the horizontal plate, resulting in a cross-sectional profile that was approximately semi-circular in shape.

To better visualize the physical configuration of the printing system, a 3D schematic model of the setup was constructed and rendered to produce the schematic shown in Figure 2. This schematic illustrates the dimensional simplification process from the full 3D printing environment to the 2D FEM model and visualizes the boundary conditions and computational mesh used for simulation. To analyze the geometric variation of the deposited filament, the developed FEM model was based on a semi-circular filament cross-section with variable diameter (d). To ensure the accuracy of the calculation, the ambient air domain near the filament was also incorporated, as it forms an essential part of the entire printing space. Since the filament cross-section and the ambient air domain showed a mirror symmetry, only half of the geometry was modeled in 2D, with a symmetry boundary condition applied to improve modeling efficiency. Geometrical features, such as shallow grooves and chamfers, were omitted to further improve the calculation efficiency. The final computational mesh, auto-generated by COMSOL, comprised 14,090 domain elements.

To estimate the swelling–shrinking behavior of hydrogel filaments, a moving mesh was employed in the FEM model to represent both the computational mesh of the printed filament and the ambient air domain within a two-phase flow framework. Given that the majority of the hydrogel's volume consisted of liquid, the printed filament was modeled as the first liquid phase. The adjacent ambient air domain, composed of moist air, was defined as the other liquid phase. The interface between the hydrogel filament and the ambient air was treated as a fluid–fluid boundary, while the outer boundary of the air domain was regarded as an outlet boundary.

The printing platform used in this study was equipped with a high-precision temperature control system (±1°C), enabling stable thermal conditions at the filament–substrate interface. Consequently, the top surface of the plate was considered a cold source. The material parameters of the hydrogel (e.g., diffusion coefficient, viscosity, and thermal conductivity), although known to be temperature-dependent, were treated as constant values corresponding to room temperature, based on steady-state data from the literature. For the filament material, a well-acclaimed medical hydrogel material, F-127, was adopted in the FEM model. The simulation parameters are summarized in Table 1. To investigate the swelling–shrinking behavior of filaments under varying humidity conditions, a series

Table 1. Selected simulation parameters

Component	Material	Thermal conductivity (W/m/K)	Dynamic viscosity (Pa·s)	Thermal capacity (J/kg/K)	Density (kg/m^3)
Ambient air	Air	0.0267	17.90×10^{-6}	1005	1.225
Printed filament	F-127	0.250	1.00×10^{-1}	4200	1095
Plate	Polymethyl methacrylate	0.192	–	1465	1180

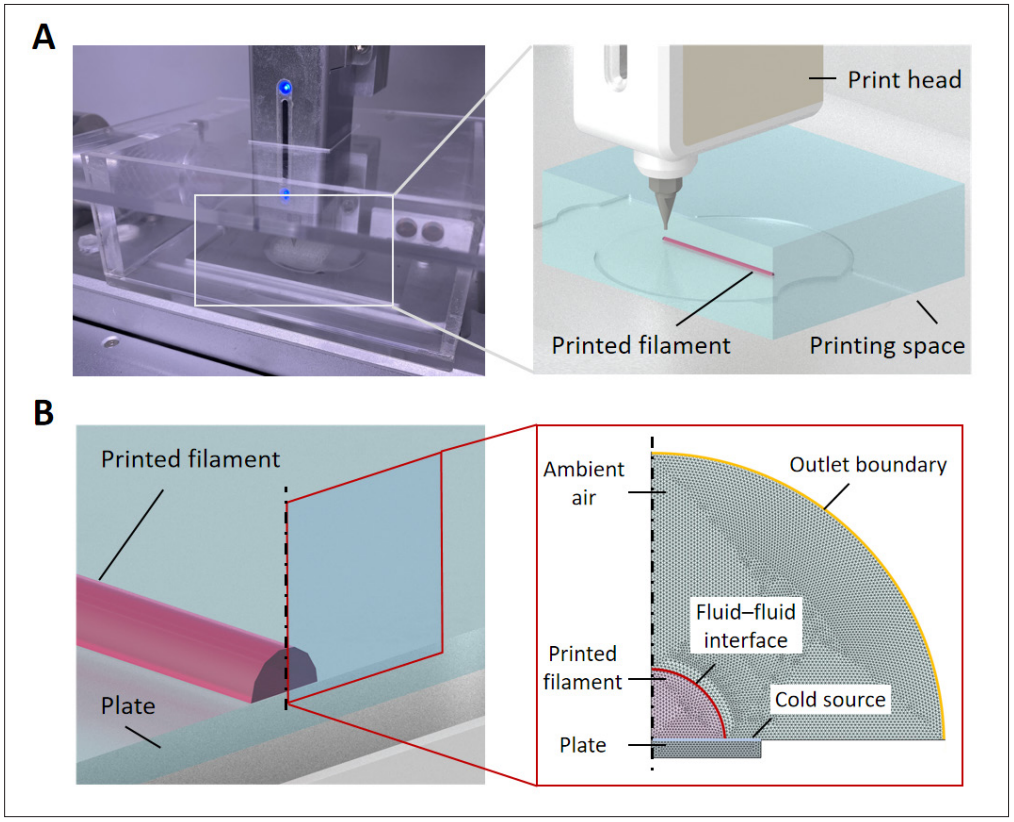

Figure 2. Finite element method modeling for investigating the humidity-driven swelling–shrinking behavior of hydrogel filaments. (A) Schematic diagram showing the extrusion process of a hydrogel filament. (B) Simplified model and computational mesh of the printed filament.

of analyses were conducted across various diameters and relative humidity (RH) values.

2.2. The boundary conditions of the finite element method modeling

2.2.1. Two-phase flow modeling of the printed filament

To simulate the swelling–shrinking behavior of hydrogel filaments under varying ambient RH conditions, the two-phase flow method was employed in the FEM model. A phase field method is suitable for modeling two immiscible fluids with stable interfaces. It enables a sharp transition between the two fluid phases, resulting in a high-resolution representation of the fluid–fluid interface. The dynamics of two-phase flow is governed by a widely adopted Cahn–Hilliard theory[35]:

$$\frac{\partial \phi}{\partial t} + u \cdot \nabla \phi = \nabla \cdot \frac{\gamma \lambda}{\omega^2} \nabla \Psi \quad \text{(I)}$$

$$\Psi = -\nabla \cdot \omega^2 \nabla \phi + (\phi^2 - 1)\phi \quad \text{(II)}$$

where ϕ is the dimensionless phase field variable, which takes a value of 1 or −1 to distinguish one fluid phase from another; $\boldsymbol{u}$ is the velocity vector; γ is the mobility rate, which determines the time scale of the Cahn–Hilliard diffusion; λ and ω are the mixing energy density and the interface thickness parameter, respectively, which are both highly related to the materials; and Ψ is the phase field auxiliary variable. These parameters were calculated in the COMSOL software without artificial settings.

2.2.2. Flow condition of the ambient air

To conduct further analysis based on the two-phase flow model, the flow conditions within the ambient air were also considered. During the evaporation process of the printed filament, water contained within the hydrogel filament diffuses into the ambient air and transitions into vapor. Conversely, water vapor from the ambient air is absorbed into the hydrogel during the swelling process. This transfer of water vapor results in a slight flow of moist air within the ambient air domain. The Reynolds number (R_e) was employed to determine this type of flow condition[36]:

$$R_e = \frac{\rho u L}{\mu} \quad \text{(III)}$$

where ρ is the density of moist air;u is the flow speed; μ is the dynamic viscosity of the fluid; and L is the characteristic length, which can be estimated according to the proposed FEM model:

$$L = \frac{D_1 + D_2}{2} \quad \text{(IV)}$$

where D_1 and D_2 are the diameters of the printed filament and the ambient air domain, respectively. Given the low speed of the moist airflow, the value of R_e was estimated to be lower than 2300. It implies that the flow condition of the ambient air should be defined as laminar flow in the FEM model. Furthermore, as the density of fluid exhibits little fluctuation with pressure in the model, the laminar flow in the ambient air domain was regarded as incompressible.

2.2.3. Cold source of the plate

According to the configuration presented in Figure 1, hydrogel filaments are deposited onto a temperature-controlled plate during the 3D printing of hydrogel architectures. Hence, the top surface of the plate, represented as a cold source in Figure 2, was defined as a temperature boundary. Specifically, the initial temperatures of the plate, the ambient air, and the printed filament were all set to room temperature in the FEM model.

2.2.4. Water vapor transport at the fluid–fluid interface

When hydrogel filaments are exposed to ambient air with inappropriate RH levels, moisture exchange between the hydrogel filaments and the surrounding environment often results in swelling or shrinking of the filaments. To account for water vapor transport across the fluid–fluid interface, the transport of diluted species model was utilized in the FEM simulation. To achieve the calculation of the diffusion and the convection process of water vapor, a widely adopted mass conservation equation, which is associated with Fick's laws of diffusion,[37] was employed:

$$\frac{\partial c}{\partial t} + \nabla \cdot \mathbf{J} + \mathbf{u} \cdot \nabla c = 0 \quad \text{(V)}$$

$$\mathbf{J} = -D' \nabla c \quad \text{(VI)}$$

where c is the concentration of water vapor; D' denotes the diffusion coefficient; and **J** is the diffusive flux vector, which measures the amount of substance that flows through a unit area during a unit time interval.

According to the mass conservation equation (**Equation V**), directly using RH as an input parameter in the calculation is impractical. Hence, to analyze geometric variations under a variety of RH conditions, the relationship between the vapor concentration and RH must be clarified[38]:

$$RH = \frac{c_v}{c_{sat}} \quad \text{(VII)}$$

where the c_v and c_{sat} are the concentration and saturation concentration of water vapor, respectively. When defining RH in the FEM model, a conversion from RH to c_v must be implemented in advance. By inputting the calculated c_v and corresponding c_{sat} into the simulation, the geometric variation of printed filaments under various ambient RH conditions can be calculated. In the model, the c_v was set to the same value for both the ambient air and the outlet boundary.

2.3. Preparation of hydrogel filaments for experimental validation

To validate the reliability of the calculation results, printing trials were conducted using hydrogel filaments. F-127, selected for these trials, is a well-acclaimed medical hydrogel material in regenerative medicine due to its excellent biodegradation properties and outstanding biocompatibility.

In this study, a 30% (w/v) F-127 solution was prepared for the 3D printing experiments. Specifically, the mixture of 1.5 g F-127 powder (P2443-1KG, Sigma-Aldrich, USA) and 5 mL phosphate-buffered saline (Thermo Fisher Scientific Inc., USA) was prepared and stored at 4°C for 24 h. Before each 3D printing, the prepared 30% (w/v) F-127 solution was transferred into syringes and centrifuged for 10 min at 4°C to remove air bubbles within the hydrogel material. Hydrogel filaments with diameters of 0.2, 0.3, and 0.4 mm were then extruded using a self-designed high-precision 3D printing device. A humidity-controlled enclosure was used to maintain a constant ambient RH for hydrogel filaments during and after the deposition process. To evaluate the geometric variation of the printed filaments under the RH of 50, 60, 70, 80, and 90%, an electronic digital microscope (Inskam-316, Aomekie, China) was employed to capture micrographs of the filament cross-sections. Representative geometric variations of hydrogel

filaments with various diameters under the RH of 50% are demonstrated in Figure 3.

2.4. Preparation of 3D-printed ear model

The widely adopted F-127 hydrogel was employed for the 3D printing trials. Before the experiment, the 30% (w/v) F-127 solution was prepared and stained with red ink to facilitate the microscopic observation of the printed structures. Three digital models of human ears with identical shapes but various sizes were designed, with a height ratio of 2:3:4. For the smallest ear model, F-127 was extruded through a 0.2 mm nozzle under ambient RH levels of 90 and 80%. For the medium-sized ear model, a 0.3 mm nozzle was adopted, and the ambient RH was controlled at 80 and 70%. Lastly, for the largest ear model, F-127 material was printed employing a 0.4 mm nozzle under the ambient RH of 60 and 50%. To evaluate the print quality of each 3D architecture, photographs of the overall view were taken using an electronic digital microscope (Inskam-316, Aomekie, USA), while top-view micrographs were taken using an optical microscope (PH50-3A43L-A1600X, Phenix, China).

2.5. Statistical analysis

All experimental results were obtained from at least three independent replicates. For each group, data are presented as mean ± standard deviation. Statistical significance was evaluated using one-way analysis of variance (ANOVA) followed by Tukey's Honestly Significant Difference test for post-hoc comparisons. A p-value < 0.05 was considered statistically significant.

3. Results and discussion

3.1. Analysis of the calculation results

The numerical investigation of the humidity-driven swelling–shrinking behavior was conducted based on three types of printed filaments with diameters of 0.2, 0.3, and 0.4 mm. For the evaporation process of each hydrogel filament, the initial RH was set to 50, 60, 70, 80, and 90%. To mimic the actual working conditions of the extrusion process, the cold source and room temperature were set to 25°C.

Figure 4 illustrates the transient-state RH distribution in the ambient air of the 0.2 mm filaments. The continuous movement of the fluid–fluid interface reflects the geometric variation of each hydrogel filament during the evaporation process. As presented in the figure, high-humidity moist air is gathered near the printed filament. Due to the water vapor diffusion from the hydrogel material, the humidity field in the ambient air domain demonstrates a

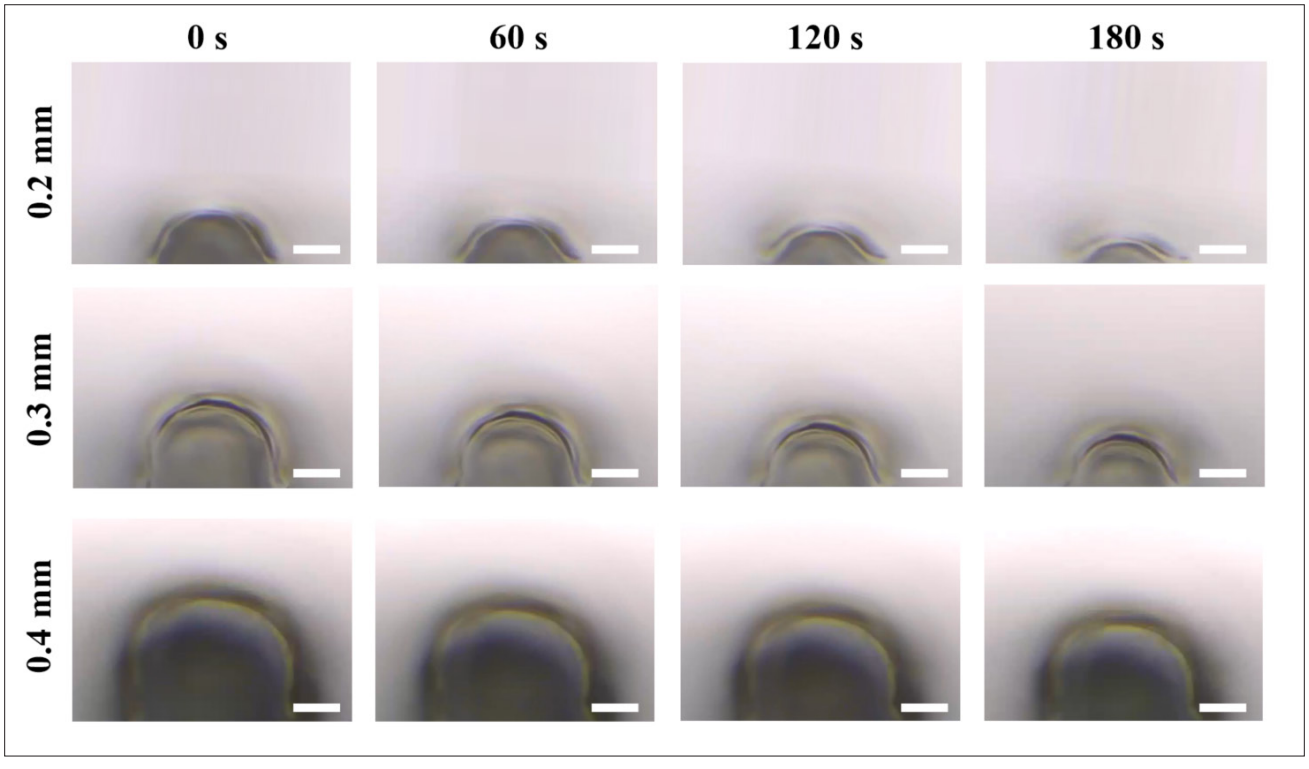

Figure 3. Micrographs of deposited hydrogel filaments with various diameters under a relative humidity of 50%. Scale bar: 0.1 mm; Magnification: 64×.

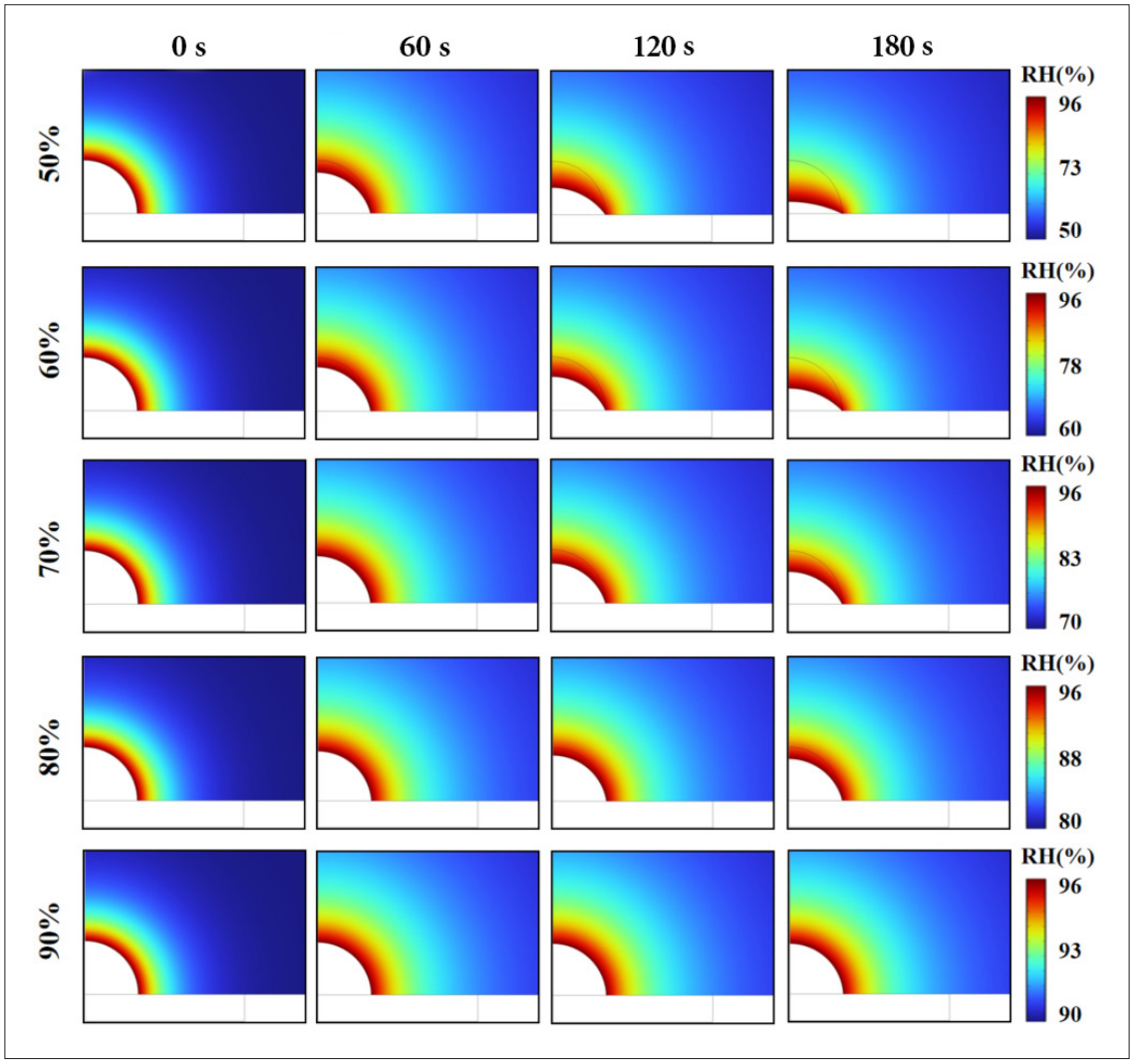

Figure 4. Humidity distribution in the ambient air with a filament diameter of 0.2 mm, illustrating the geometric variation of the printed filament under various relative humidity (RH) conditions.

moisture gradient in the radial direction. When the RH is defined to a low value, such as 50%, the rate of moisture loss is significantly increased, leading to the most severe geometric shrinkage of the printed filament.

The process from deposition to the complete collapse of the entire hydrogel structure lasts for approximately 180 s. Given that 3D printing of large-scale architectures is typically time-consuming, such a rapid geometric decrease is unacceptable during the fabrication process. As the ambient RH increases, the concentration of water in the ambient air approaches that within the hydrogel filament. This leads to insufficient moisture transfer and vapor diffusion, moderating the geometric shrinkage of the just-printed hydrogel filaments. Figure 5 and 6 demonstrate the geometric variations of the 0.3 and 0.4 mm filaments, respectively.

With increasing filament diameter, the geometric shrinkage of the hydrogel filaments is alleviated. Among the three types of hydrogel filaments with various diameters, the 0.4 mm filament exhibits the largest initial volume and contains the greatest amount of water. This implies a higher moisture retention capacity during the evaporation process. Therefore, compared with the 0.2 and 0.3 mm filaments, the 0.4 mm filament demonstrates superior shape stability when exposed to moist air at the same RH.

As the RH increases, both the 0.3 and 0.4 mm filaments ultimately demonstrate swelling behavior. When the

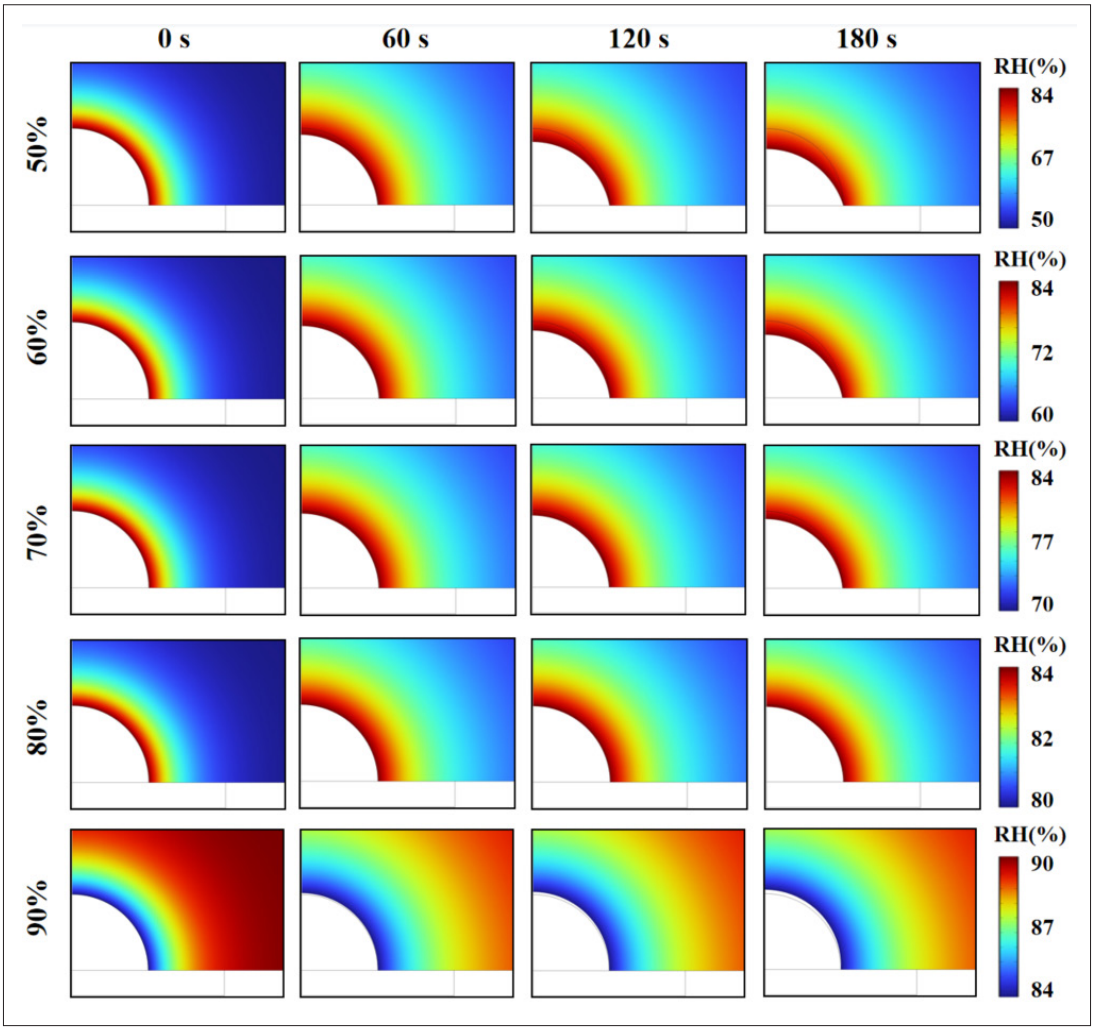

Figure 5. Humidity distribution in the ambient air with a filament diameter of 0.3 mm, illustrating the geometric variation of the printed filament under various relative humidity (RH) conditions.

concentration of water vapor in the ambient air exceeds that within the hydrogel, moisture absorption occurs at the fluid–fluid interface, leading to geometric swelling of the printed filaments.[39]

The swelling–shrinking behavior of printed filaments was quantitatively compared and investigated (Figure 7). As demonstrated in Figure 7A, the original and deformed shapes of the filament are outlined separately using dashed lines. During the humidity-driven geometric transforming process, the height of each printed filament was measured and symbolized as "H2," while the height of the original shape of the filament was symbolized as "H1," which corresponded to the radius of the original filament. To quantitatively evaluate the extent of geometric shrinkage, the ratio of H2 to H1 was calculated for each printed filament.

As demonstrated in Figure 7B, five geometric variation curves are obtained for the 0.2 mm filament. All curves display a clear linear reduction over time, with the most pronounced shrinkage observed at an RH of 50%. Likewise, the geometric variation curves of the 0.3 mm filament, as presented in Figure 7C, show similar trends when the RH is not more than 80%. However, the geometric variation curve exhibits an increasing trend at an RH of 90%. In Figure 7D, linear increases in the curves of 0.4 mm filaments occur when the RH is not lower than 70%, with the most prominent swelling occurring at 90% RH.

Generally, significant geometric variations of extruded filaments are not permitted in the manufacturing of 3D biomimetic architectures.[40] To meet the strict requirements of medical applications, deviations between the size of the shrinking filament and that of the original

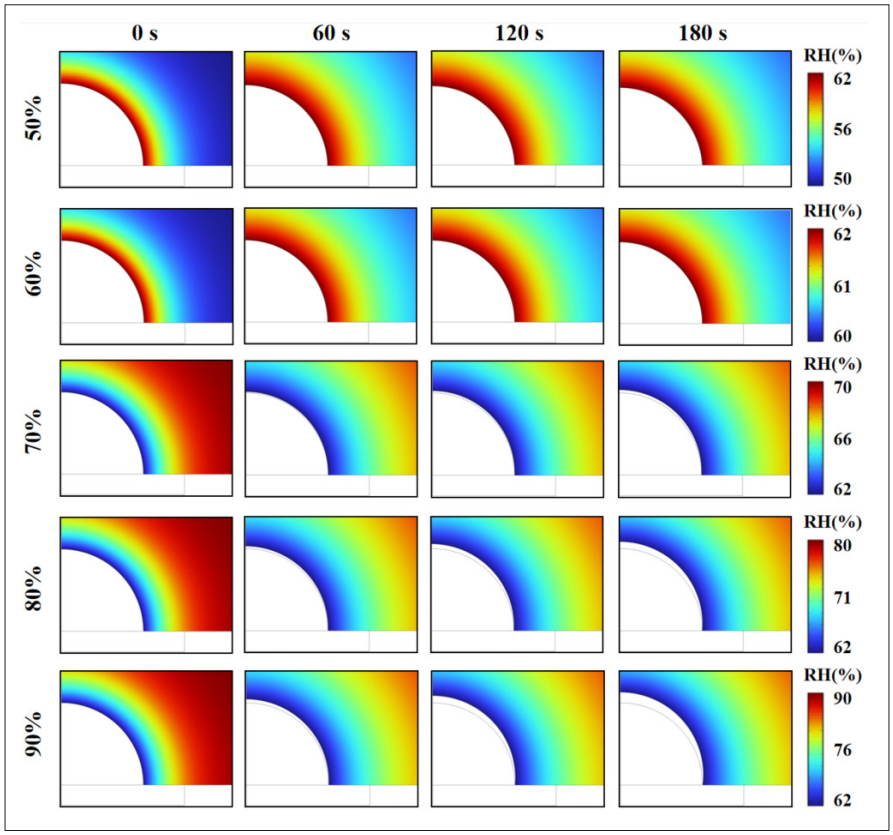

Figure 6. Humidity distribution in the ambient air with a filament diameter of 0.4 mm, illustrating the geometric variation of the printed filament under various relative humidity (RH) conditions.

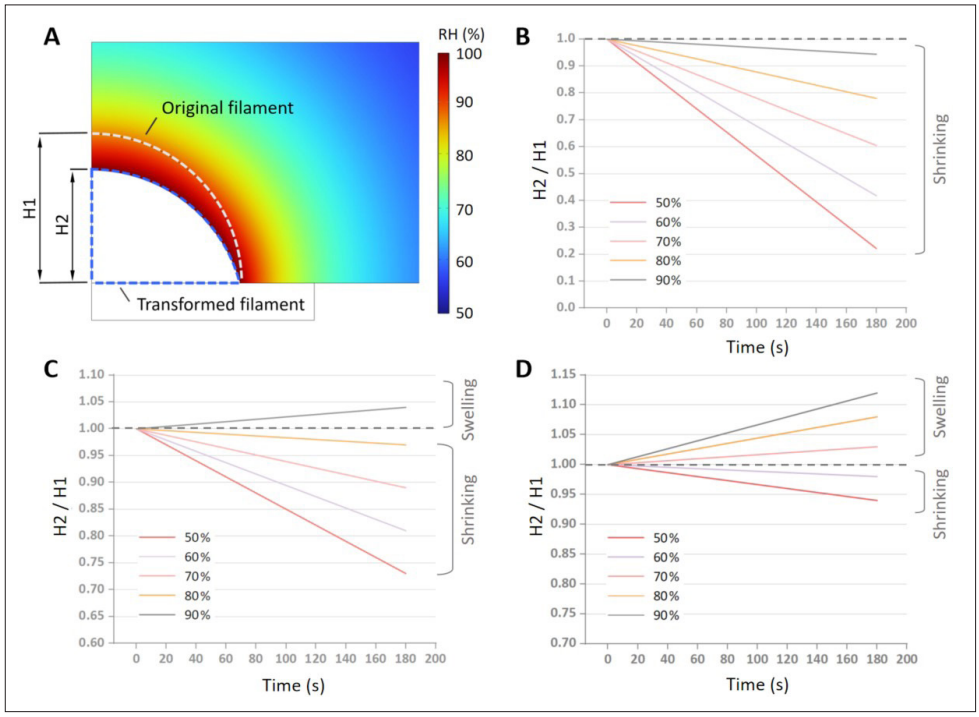

Figure 7. Quantitative comparison of the geometric variation of the printed filaments. (A) Schematic diagram of the transformed filament in the finite element method model. (B–D) Geometric variation curves of the printed filaments with various diameters: (B) 0.2 mm, (C) 0.3 mm, and (D) 0.4 mm.

filament should be minimized. To identify the optimal RH levels for hydrogel 3D printing, horizontal dashed lines corresponding to an H2/H1 of 1 are included in Figure 7B–D. The geometric variation of the 0.2 mm filament reaches the greatest moderation at 90% RH. For the 0.3 mm filament, both the curves of the 80 and 90% RHs demonstrate lower deviations from the dashed line. Similarly, for the 0.4 mm filament, the geometric variation presents the lowest alleviation at 60 and 70% RHs.

In practice, the challenges posed by humidity-driven swelling are more severe than those of humidity-driven shrinking. During the layer-by-layer deposition process, well-arranged hydrogel filaments in adjacent layers fuse, creating an architecture with a larger volume. When the RH is too low, shrinking filaments reduce structural density and slightly weaken the mechanical properties of the manufactured 3D structure. However, due to the fusion of hydrogel filaments, the moisture transfer between adjacent filaments can partially moderate the impact of moisture loss. In contrast, when the RH is excessively high, swelling filaments reduce the spacing between adjacent filaments, lowering the pore size within the 3D architecture. This can not only cause uncontrolled mechanical properties but also lead to poor breathability, limiting the applicability of the biomimetic structure in cell culturing or tissue engineering.

Therefore, based on the deformation trends obtained from the simulations, the RH level corresponding to the minimal deviation from an H2/H1 of 1 was selected as the optimal RH for each filament diameter. According to the calculation results, the optimal RH levels for the 3D printing process of the 0.2, 0.3, and 0.4 mm hydrogel filaments were 90, 80, and 60%, respectively.

3.2. Experimental validation of the simulation results

As demonstrated in Figure 8A, the height of the 3D-printed F-127 filament was measured from the captured micrographs. By calculating the H2-to-H1 ratio based on the micrographs, the geometric variation curves of 0.2, 0.3, and 0.4 mm F-127 filaments were plotted (Figure 8B–D). When compared with the simulation results in Figure 6, although the experimental curves do not perfectly match the simulated data, the overall trends show strong agreement. To measure the deviation of the experimental results from the simulated data, absolute errors (ε) between the simulated and the experimental geometric variation curves were calculated at several time points (Table 2).

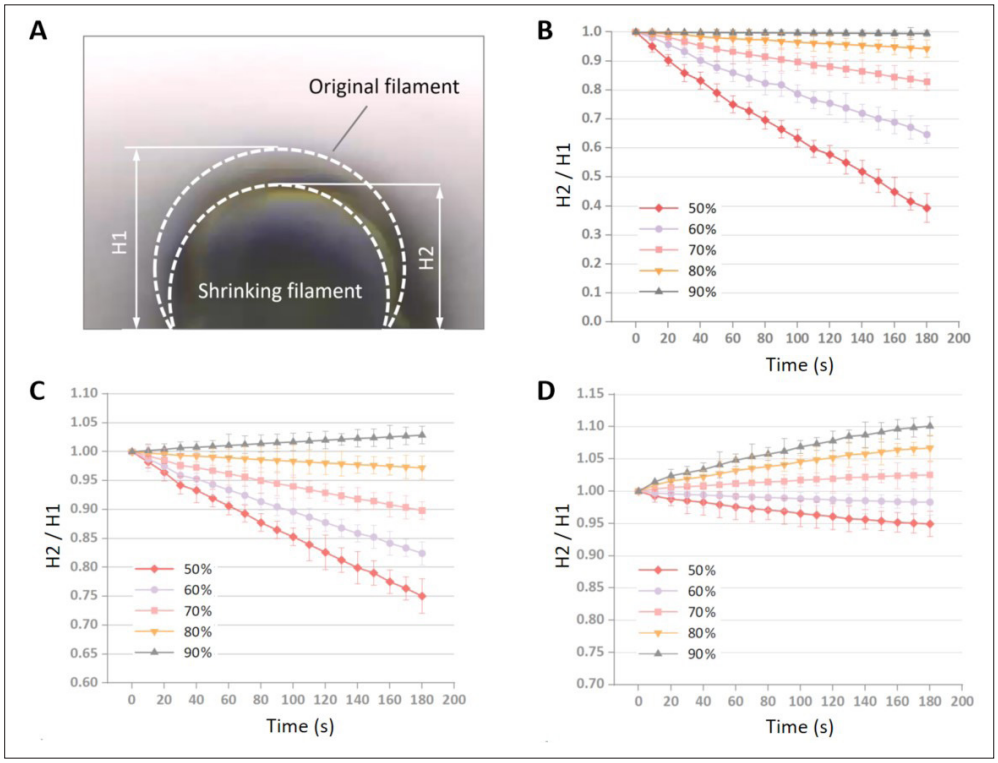

Figure 8. Geometric variation curves of the 3D-printed hydrogel filaments. (A) Schematic diagram of the measurement of filament diameters. (B–D) Geometric variation curves of hydrogel filaments with various diameters: (B) 0.2 mm, (C) 0.3 mm, and (D) 0.4 mm.

Compared with the simulated curves in Figure 6, the variation of each experimental curve in Figure 8 is not strictly linear. Instead, all experimental curves exhibit a decreasing rate of descent over time, resulting in increasing deviation between the experimental and simulation data. This phenomenon can be attributed to the unique internal structure of hydrogel materials, which consists of a fluid phase (water) and a solid phase (crosslinked polymer network). During moisture loss, the polymer network remains within the filament, playing the role of load-bearing and shape-retaining. At the beginning of evaporation, the polymer network constitutes a small volume of the hydrogel filament and thus has little impact on geometric variation. However, as water content in the material decreases, the proportion of the solid phase increases. Consequently, the influence of moisture loss on geometric shrinkage is gradually alleviated as H2/H1 decreases, eventually leading to a greater ε. Nevertheless, although neglecting the polymer network causes a gentle increase in ε, the simulation results still match the experimental data well in most cases. As shown in Table 2, the maximum absolute error (ε_{Max}) across geometric variation curves is limited to 0.228, supporting the reliability of the FEM simulation results.

3.3. 3D printing trial for hydrogel filaments under optimal humidity

Due to the remarkable humidity-driven swelling–shrinking behavior of hydrogels, inappropriate RH levels within the printing space can severely affect the layer-by-layer deposition of complex 3D architectures. To address this issue, the present method aims to identify optimal RH levels for 3D printing hydrogel filaments and to alleviate the collapse or shrinkage of multilayered constructs. According to the FEM simulation result, the optimal RH levels for the 0.2, 0.3, and 0.4 mm hydrogel filaments are 90, 80, and 60%, respectively. To validate the feasibility of these conditions, 3D hydrogel architectures were manufactured using the 3D printer shown in Figure 1, and the corresponding results are presented in this section.

Figure 9A–C demonstrates 3D-printed ear models of small, medium, and large sizes, respectively, fabricated

Table 2. The absolute error and the maximum absolute error between the simulated data and the experimental results across multiple time points

d (mm)	RH (%)	ε									ε_{Max}
		20 s	40 s	60 s	80 s	100 s	120 s	140 s	160 s	180 s	
0.2	50	0.024	0.015	0.015	0.015	0.040	0.076	0.110	0.134	0.171	0.171
	60	0.012	0.017	0.035	0.062	0.091	0.127	0.162	0.202	0.228	0.228
	70	0.019	0.030	0.050	0.076	0.103	0.133	0.164	0.193	0.224	0.224
	80	0.015	0.027	0.043	0.064	0.080	0.101	0.122	0.143	0.162	0.162
	90	0.005	0.010	0.015	0.021	0.027	0.033	0.039	0.045	0.051	0.051
0.3	50	0.008	0.010	0.008	0.007	0.002	0.002	0.006	0.013	0.021	0.021
	60	0.006	0.007	0.006	0.005	0.002	0.001	0.004	0.009	0.014	0.014
	70	0.003	0.004	0.003	0.003	0.001	0.001	0.002	0.005	0.008	0.008
	80	0.001	0.001	0.001	0.001	0.001	0.002	0.005	0.002	0.002	0.005
	90	0.001	0.001	0.002	0.003	0.005	0.006	0.007	0.009	0.011	0.011
0.4	50	0.006	0.004	0.004	0.003	0.002	0.001	0.003	0.005	0.009	0.009
	60	0.002	0.002	0.002	0.001	0.001	0.001	0.001	0.002	0.003	0.003
	70	0.003	0.002	0.002	0.001	0.001	0.003	0.001	0.002	0.005	0.005
	80	0.007	0.005	0.006	0.004	0.002	0.001	0.003	0.006	0.012	0.012
	90	0.011	0.008	0.009	0.005	0.003	0.001	0.005	0.009	0.019	0.019

Abbreviations: *d*:, diameter; RH, relative humidity.

under optimal RH conditions of 90, 80, and 60%. Under these conditions, the constructs maintained splendid shape throughout the 3D printing process. The well-arranged F-127 filaments provided stable support for adjacent layers and exhibited smooth, uniform shapes. In contrast, Figure 9D–F presents ear models printed under inappropriate ambient RH conditions of 80, 70, and 50% for the small, medium, and large sizes, respectively. Although the F-127 hydrogel filaments initially appeared continuous upon deposition, as printing proceeded, a gradual shrinkage and even collapse occurred due to inappropriate ambient RH. This compromised the capability to support the upper layers and resulted in irregular holes within the 3D-printed architectures. At the edges of each model, an evident moisture loss occurred, as demonstrated in the micrographs. These fragile structures often fail to provide the mechanical or biological properties required for medical applications.

The observed phenomena can be explained as follows. The medical-grade biodegradable hydrogel used in this study consists of hydrophilic polymer networks that retain plenty of water and exhibit pronounced humidity-driven swelling–shrinking behavior. As illustrated in Figure 6, to minimize moisture loss and geometric variation of the hydrogel filaments, specific RH levels were selected as the optimal RH for each filament diameter. Since the ear models (Figure 9A–C) were printed under these selected RH conditions, the shape of each hydrogel filament was maintained throughout the manufacturing process. On the contrary, when the ambient RH was inappropriate (Figure 9D–F), the moisture loss led to geometric shrinkage.

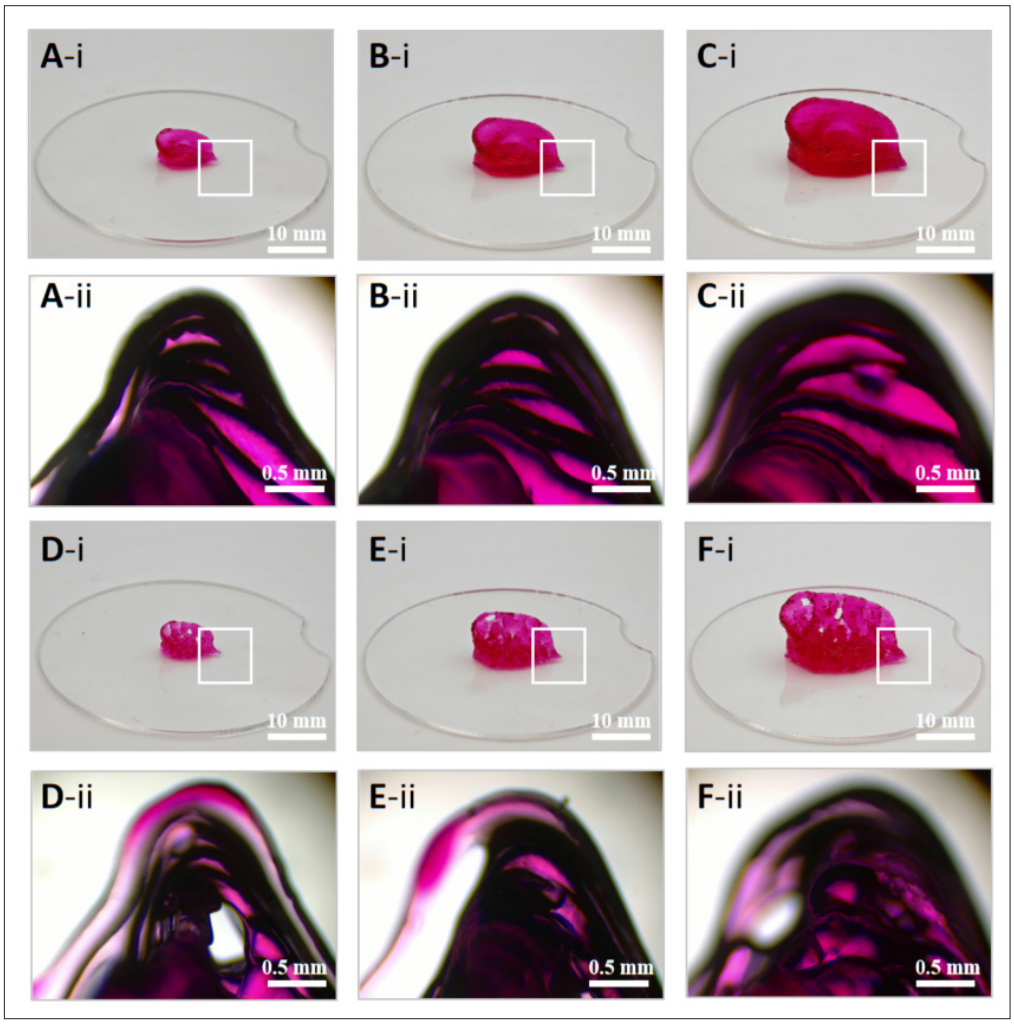

Figure 9. Photographs and micrographs of the 3D-printed ear models. (A–C) Ear models printed with filament diameters of (A) 0.2 mm, (B) 0.3 mm, and (C) 0.4 mm under optimal ambient humidity conditions. (D–F) Corresponding models printed under relatively low ambient humidity conditions, showing structural deformation. Scale bar for all upper panels: 10 mm; Magnification: 8×. Scale bar for all lower panels: 0.5 mm; Magnification: 64×.

To provide a quantitative basis for evaluating the printing quality of the hydrogel constructs under different RH conditions, the overall height of each printed structure was measured as a representative indicator of structural integrity. Given the complexity of the ear-shaped geometry, conventional image analysis techniques, such as edge detection, contour extraction, or pixel-wise segmentation, were not feasible for consistent quantitative assessment. Therefore, vertical height was selected as a measurable and reproducible metric that reflects the degree of structural collapse or swelling caused by humidity-driven deformation. The height of each sample was obtained from side-view images and is presented in Table 3. The results demonstrate that samples printed under optimal RH conditions exhibited significantly greater structural retention compared to those printed under inappropriate RH conditions.

Currently, numerous studies have explored 3D printing using F-127 materials. However, a majority of these printed structures exhibit shrinkage and collapse during the extrusion process due to inappropriate ambient RH. Moisture loss significantly limits the fabrication of large-scale 3D architectures with complex structures. Table 4 compares the 3D-printed F-127 architectures of various sizes in existing studies. It demonstrates that the effective lengths and widths of recently proposed structures usually fall within the range of 5–10 mm, with effective heights generally not higher than 8 mm. Meanwhile, the shapes of these architectures are not complex enough to meet the requirements of medical applications. In contrast, in this study, a 3D-printed ear model with an effective size of 20 mm (length) × 10 mm (width) × 10 mm (height) is successfully generated. This outcome confirms that 3D printing with optimal RH conditions can alleviate moisture loss and enhance the structural fidelity of 3D architectures.

F-127 was selected as the model hydrogel in this study due to its pronounced and stable geometric deformation under varying RH conditions, along with its excellent printability and reproducibility. These characteristics made it suitable for controlled investigation of humidity-driven swelling–shrinking mechanisms and for quantitative FEM modeling. However, it is important to note that the proposed finite element framework—including two-phase flow modeling, water vapor transport simulation, and RH–geometry coupling—is not limited to the specific material properties of F-127. The model is designed to be generalizable and can be applied to other widely used hydrogel-based inks, such as GelMA with tunable crosslinking density, ionically crosslinked alginate, and photopolymerizable PEG-DA, provided that key physical parameters (e.g., swelling ratio, viscosity, and diffusion coefficient) are available. These hydrogels are extensively used in tissue engineering and bioprinting, indicating the strong applicability and scalability of our model in practical biomanufacturing settings.

4. Conclusion

In this study, the humidity-driven swelling–shrinking behavior of hydrogel filaments during 3D printing was investigated through numerical simulations and experimental validation. A novel FEM coupling field simulation model was developed to identify optimal

Table 3. Overall heights of printed structures with various humidity levels

Figure	Filament diameter (mm)	Ambient humidity (%)	Overall height (mm)
A	0.2	90	5.4
D		80	4.5
B	0.3	80	8.5
E		70	7.6
C	0.4	60	10.0
F		50	8.8

Table 4. Results of printed F-127 structures in recent studies

Reference	Structure	Filament diameter (mm)	Effective size (length × width × height, mm^3)
[41]	Reticulate structure	0.5	8×8×1
[42]		0.2	10×10×5
[43]	Cube structure	0.4	5×5×5
	Pyramid structure		10×10×8

ambient RH conditions for hydrogel extrusion. Printing trials were conducted to validate the effectiveness of the proposed approach in mitigating geometric shrinkage in 3D-printed architectures. The main conclusions are summarized as follows:

(i) A FEM thermal–humidity–multiphase flow coupling field simulation model was proposed and experimentally validated, successfully predicting the geometric variation of hydrogel filaments under a variety of ambient RH conditions.

(ii) The optimal RH conditions for 3D printing of hydrogel filaments with diameters of 0.2, 0.3, and 0.4 mm were identified as 90, 80, and 60%, respectively.

(iii) Printing trials using F-127 hydrogel materials demonstrated that higher ambient RH effectively prevents both uncontrollable geometric swelling and shrinkage during the 3D printing process.

(iv) Under optimized RH conditions for hydrogel filaments, 3D architectures of the human ear were successfully manufactured with an effective size of 20 mm (length) × 10 mm (width) × 10 mm (height).

It should be noted that the humidity-driven swelling–shrinking behavior discussed in this study is specific to hydrogel-based biomaterials, such as F-127 and GelMA. These materials possess high water content and strong moisture responsiveness under ambient conditions. In contrast, thermoplastic biocompatible polymers, such as polycaprolactone and polypropylene, are largely unaffected by humidity due to their hydrophobic nature and low water uptake. Therefore, the findings of this study are not intended to generalize across all biocompatible printing materials.

Although the present study provides a quantitative understanding of humidity-driven deformation in single-layer hydrogel filaments, the current model is limited to 2D cross-sectional simulations and does not fully capture the 3D deposition dynamics of multilayer structures. In practice, interlayer moisture transport, filament fusion behavior, and cumulative deformation significantly impact the final geometry and functionality of printed biomimetic constructs. Due to the absence of robust theoretical models for describing layer-by-layer coupling and time-dependent structural evolution, accurate simulation of full 3D architectures remains a challenge. Future work will focus on developing a comprehensive, multi-physics 3D FEM framework that incorporates interlayer interactions and global deformation mechanisms. This will further enhance the predictive capability and practical value of the proposed approach in large-scale hydrogel biomanufacturing.

Acknowledgments

None.

Funding

The authors deeply acknowledge the financial support from the Key Research and Development Plan Project of Heilongjiang Province (grant no. 2022ZX02C22); the Science and Technology Innovation Talent Project on Manufacturing Industry of Harbin (grant no. 2023HBRCGD011, 2022CXRCGD029); the Interdisciplinary Research Foundation of HIT (grant no. IR2021223); and the Natural Science Foundation of Chongqing (grant no. CSTB2023NSCQ-MSX0822).

Conflict of interest

Dr. Swee Leong Sing serves as the Editorial Board Member of the journal, but did not in any way involve in the editorial and peer-review process conducted for this paper, directly or indirectly. Other authors declare they have no competing interests.

Author contributions

Conceptualization: Qiang Gao
Data curation: Qiang Gao
Formal analysis: Lihua Lu
Funding acquisition: Wei Zhang
Investigation: Peng Zhang
Methodology: Min Zhu
Project administration: Lihua Lu
Resources: Le Xu
Software: Kaicheng Yu
Supervision: Yifeng Yao
Validation: Swee Leong Sing
Visualization: Wei Zhang
Writing–original draft: Kaicheng Yu
Writing–review and editing: Kaicheng Yu

Ethics approval and consent to participate

Not applicable.

Consent for publication

Not applicable.

Availability of data

The datasets generated and analyzed during the current study are available from the corresponding author upon reasonable request.

Reference

1 Kühl J, Gorb S, Kern M, et al. Extrusion-based 3D printing of osteoinductive scaffolds with a spongiosa-inspired structure. *Front Bioeng Biotechnol*. 2023;11:1268049. doi: 10.3389/fbioe.2023.1268049.

2. Dutta SD, An JM, Hexiu J, et al. 3D bioprinting of engineered exosomes secreted from M2-polarized macrophages through immunomodulatory biomaterial promotes in vivo wound healing and angiogenesis. *Bioact Mater.* 2025;45:345-362. doi: 10.1016/j.bioactmat.2024.11.026.

3. Daly AC, Prendergast ME, Hughes AJ, Burdick JA. Bioprinting for the biologist. *Cell*. 2021;184(1):18-32. doi: 10.1016/j.cell.2020.12.002.

4. Wang H, Guo K, Zhang L, et al. Valve-based consecutive bioprinting method for multimaterial tissue-like constructs with controllable interfaces. *Biofabrication*. 2021;13:035001. doi: 10.1088/1758-5090/abdb86.

5. Zhao Z, Xiang Y, Koellhoffer EC, et al. 3D bioprinting cowpea mosaic virus as an immunotherapy depot for ovarian cancer prevention in a preclinical mouse model. *Mater Adv*. 2024;5(4):1480-1486. doi: 10.1039/D3MA00899A.

6. Weng T, Zhang W, Xia Y, et al. 3D bioprinting for skin tissue engineering: current status and perspectives. *J Tissue Eng*. 2021;12:1758518878. doi: 10.1177/20417314211028574.

7. Ng WL, An J, Chua CK. Process, material, and regulatory considerations for 3D printed medical devices and tissue constructs. *Engineering*. 2024;36:146-166. doi: 10.1016/j.eng.2024.01.028.

8. Namazi AM, Aghajanzadeh MS, Imani R. Optimizing a self-healing gelatin/aldehyde-modified xanthan gum hydrogel for extrusion-based 3D printing in biomedical applications. *Mater Today Chem*. 2024;40:102208. doi: 10.1016/j.mtchem.2024.102208.

9. Ijeoma P, Ridel AF, Parkar H. Digital protocol for the bioprinting of a three-dimensional acellular dermal scaffold. Biomedical visualization. In: *How to use 3D Printing Innovations and Digital Storage to Democratize Anatomy Education*. Biomedical Visualization, Springer, Cham. 2024:99-113. doi: 10.1007/978-3-031-68501-9_5.

10. Li W, Wang M, Ma H, Chapa-Villarreal FA, Lobo AO, Zhang YS. Stereolithography apparatus and digital light processing-based 3D bioprinting for tissue fabrication. *iScience*. 2023;26(2):106039. doi: 10.1016/j.isci.2023.106039.

11. Liu J, Xu C. Improving uniformity of cell distribution in post-inkjet-based bioprinting. *J Manuf Sci Eng*. 2024;146(1):014501. doi: 10.1115/1.4063134.

12. Bozek J, Kurchakova O, Michel J, et al. Pneumatic conveying inkjet bioprinting for the processing of living cells. *Biofabrication*. 2025;17:025003. doi: 10.1088/1758-5090/ada8e2.

13. Zhang P, Gao Q, Yu K, Yao Y, Lu L. Investigation on the temperature control accuracy of a print head for extrusion 3D printing and its improved design. *Biomedicines*. 2022;10(6):1233. doi: 10.3390/biomedicines10061233.

14. Gao Q, Yu K, Chen F, Lu L, Zhang P. Investigation on the temperature distribution uniformity of an extrusion-based 3D print head and its temperature control strategy. *Pharmaceutics*. 2022;14(10):2108. doi: 10.3390/pharmaceutics14102108.

15. Ji S, Guvendiren M. Complex 3D bioprinting methods. *APL Bioeng.* 2021;5(1):11508. doi: 10.1063/5.0034901.

16. Wang X, Jiang J, Yuan C, et al. 3D bioprinting of GelMA with enhanced extrusion printability through coupling sacrificial carrageenan. *Biomater Sci.* 2024;12(3):738-747. doi: 10.1039/D3BM01489D.

17. Burns N, Rajesh A, Manjula-Basavanna A, Duraj-Thatte A. 3D extrusion bioprinting of microbial inks for biomedical applications. *Adv Drug Deliv Rev.* 2025;217:115505. doi: 10.1016/j.addr.2024.115505.

18. Iyer KS, Bao L, Zhai J, et al. Microgel-based bioink for extrusion-based 3D bioprinting and its applications in tissue engineering. *Bioact Mater*. 2025;48:273-293. doi: 10.1016/j.bioactmat.2025.02.003.

19. Yuce-Erarslan E, Tutar R, Izbudak B, et al. Photo-crosslinkable chitosan and gelatin-based nanohybrid bioinks for extrusion-based 3D-bioprinting. *Int J Polym Mater.* 2021;72(1):1-12. doi: 10.1080/00914037.2021.1981322.

20. Lima TDPL, Canelas CADA, Concha VOC, Costa FAMD, Passos MF. 3D bioprinting technology and hydrogels used in the process. *J Funct Biomater.* 2022;13(4):214. doi: 10.3390/jfb13040214.

21. Shie M, Shen Y, Astuti SD, et al. Review of polymeric materials in 4D printing biomedical applications. *Polymers*. 2019;11(11):1864. doi: 10.3390/polym11111864.

22. Chang CC, Boland ED, Williams SK, Hoying JB. Direct-write bioprinting three-dimensional biohybrid systems for future regenerative therapies. *J Biomed Mater Res B Appl Biomater*. 2011;98B(1):160-170. doi: 10.1002/jbm.b.31831.

23. Lv C, Sun X, Xia H, et al. Humidity-responsive actuation of programmable hydrogel microstructures based on 3D printing. *Sens Actuators B Chem*. 2018;259:736-744. doi: 10.1016/j.snb.2017.12.053.

24. Dai C, Li Z, Li Z, et al. Direct-printing hydrogel-based platform for humidity-driven dynamic full-color printing and holography. *Adv Funct Mater*. 2023;33(9):2212053. doi: 10.1002/adfm.202212053.

25. Sun S, Xu Y, Maimaitiyiming X. 3D printed carbon nanotube/polyaniline/gelatin flexible NH3, stress, strain, temperature multifunctional sensor. *React Funct Polym*. 2023;190:105625. doi: 10.1016/j.reactfunctpolym.2023.105625.

26. Yu K, Gao Q, Lu L, Zhang P. A process parameter design method for improving the filament diameter accuracy of extrusion 3D printing. *Materials*. 2022;15(7):2454. doi: 10.3390/ma15072454.

27. Zhao L, Wang P, Tian J, et al. A novel composite hydrogel for solar evaporation enhancement at air-water interface. *Sci Total Environ*. 2019;668:153-160. doi: 10.1016/j.scitotenv.2019.02.407.

28. Park JH, Jang J, Lee J, Cho D. Current advances in three-dimensional tissue/organ printing. *Tissue Eng Regen Med*. 2016;13:612-621. doi: 10.1007/s13770-016-8111-8.

29. Search J, Mahjoubnia A, Chen AC, et al. 3D-printing of selectively porous, freestanding structures via humidity-induced rapid phase change. *Addit Manuf*. 2023;68:103514. doi: 10.1016/j.addma.2023.103514.

30. Matamoros M, Gómez-Blanco JC, Sánchez ÁJ, et al. Temperature and humidity PID controller for a bioprinter atmospheric enclosure system. *Micromachines*. 2020;11(11):999. doi: 10.3390/mi11110999.

31. Yu K, Gao Q, Yao Y, Lin Z, Zhang P, Lu L. Investigation of the humidity control in the printing space for the material extrusion of medical biodegradable hydrogel. *Addit Manuf*. 2024;93:104452. doi: 10.1016/j.addma.2024.104452.

32. Yu K, Gao Q, Xu J, et al. Computational investigation of a 3D-printed skin substitute with orthotropy in mechanical property. *Comput Biol Med*. 2023;166:107536. doi: 10.1016/j.compbiomed.2023.107536.

33. Scotti C, Wirz D, Wolf F, et al. Engineering human cell-based, functionally integrated osteochondral grafts by biological bonding of engineered cartilage tissues to bony scaffolds. *Biomaterials*. 2010;31(8):2252-2259. doi: 10.1016/j.biomaterials.2009.11.110.

34. Cubo N, Garcia M, Del CJ, Velasco D, Jorcano JL. 3D bioprinting of functional human skin: production and in vivo analysis. *Biofabrication*. 2016;9:15006. doi: 10.1088/1758-5090/9/1/015006.

35. Cahn JW, Hilliard JE. Free energy of a nonuniform system. I. Interfacial free energy and free energy of a nonuniform system. III. Nucleation in a two-component incompressible fluid. *J Chem Phys*. 1959;31:688-699. doi: 10.1002/9781118788295.ch3.

36. Gao Q, Lu L, Zhang R, Song L, Huo D, Wang G. Investigation on the thermal behavior of an aerostatic spindle system considering multi-physics coupling effect. *Int J Adv Manuf Technol*. 2019;102:3813-3823. doi: 10.1007/s00170-019-03509-4.

37. Fick A. On liquid diffusion. *J Membr Sci*. 1995;100(1):33-38. doi: 10.1016/0376-7388(94)00230-V.

38. Shu S, Zhan Z, Xu J, Huang Y, Huang W, Lin Y. Three-dimensional numerical simulation and experiment of moisture condensation mechanism inside high voltage switchgear. *Int J Electr Power Energy Syst*. 2023;151:109129. doi: 10.1016/j.ijepes.2023.109129.

39. Naghieh S, Chen X. Printability–a key issue in extrusion-based bioprinting. *J Pharm Anal*. 2021;11(5):564-579. doi: 10.1016/j.jpha.2021.02.001.

40. Schwab A, Levato R, D Este M, Piluso S, Eglin D, Malda J. Printability and shape fidelity of bioinks in 3D bioprinting. *Chem Rev*. 2020;120(19):11028-11055. doi: 10.1021/acs.chemrev.0c00084.

41. Lee J, Kim G. Three-dimensional hierarchical nanofibrous collagen scaffold fabricated using fibrillated collagen and pluronic F-127 for regenerating bone tissue. *ACS Appl Mater Interfaces*. 2018;10(42):35801-35811. doi: 10.1021/acsami.8b14088.

42. Boonlai W, Hirun N, Suknuntha K, Tantishaiyakul V. Development and characterization of pluronic F127 and methylcellulose based hydrogels for 3D bioprinting. *Polym Bull*. 2023;80:4555-4572. doi: 10.1007/s00289-022-04271-6.

43. Fu Z, Angeline V, Sun W. Evaluation of printing parameters on 3D extrusion printing of pluronic hydrogels and machine learning guided parameter recommendation. *Int J Bioprint*. 2021;7(4):434. doi: 10.18063/ijb.v7i4.434.